Symmetry properties and bifurcations of viscoelastic thermovibrational convection in a square cavity

Alessio Boaro, Gregor MacDowall, and Marcello Lappa[*]

Department of Mechanical and Aerospace Engineering, University of Strathclyde, Glasgow G1 1XJ, United Kingdom

To fill a gap in the literature about the specific dynamics of thermovibrational flow in a square cavity filled with a viscoelastic fluid when vibrations and the imposed temperature gradient are concurrent, a parametric investigation has been conducted to investigate the response of this system over a relatively wide subregion of the space of parameters ($Pr_g = 10$; viscosity ratio $\xi = 0.5$; nondimensional frequency $\Omega = 25, 50, 75$, and 100; and $Ra_\omega \in [Ra_{\omega,cr}, 3.3 \times 10^4]$, where $Ra_{\omega,cr}$ is the critical vibrational Rayleigh number). Through solution of the governing nonlinear equations formulated in the framework of the finitely extensible nonlinear elastic Chilcott-Rallison paradigm, it is shown that the flow is prone to develop a unique hierarchy of bifurcations where initially subharmonic spatiotemporal regimes can be taken over by more complex states driven by the competition of disturbances with different symmetries if certain conditions are considered. What drives a wedge between the cases with parallel and perpendicular vibrations is essentially the existence of a threshold to be exceeded to produce convection in the former case. Nevertheless, these two configurations share some interesting properties, which are reminiscent of the resonances and antiresonances typical of multicomponent mechanical structures. Additional insights into these behaviors are gained through consideration of quantities representative of the kinetic and elastic energy globally possessed by the system and its sensitivity to the initial conditions.

I. INTRODUCTION

Vibrations are ubiquitous in engineering as liquids or gases are. These inertial disturbances can be produced by a variety of possible causes such as imbalance, misalignment, wear or looseness in machinery and other mechanical systems. More in general, they can be regarded as the outcome of any kind of external or internal force acting on a physical system that is elastic in nature or consists of a network of non–infinitely rigid parts or materials. When combined with fluids, these disturbances give rise to a specific class of fluid motions known as "vibrational flows."

These phenomena have enjoyed considerable interest since the early 2000s as they naturally complement other forms of natural convection induced by standard forces such as gravity or surface tension. Just as these forces can produce in a nonisothermal fluid "thermogravitational" or "thermocapillary" convective effects, vibrations can give rise to a different branch of this tree generally known as "thermovibrational" convection. This category of flows has attracted appreciable attention since the early 2000s as a testbed for the identification of universal principles in the dynamics of nonisothermal systems undergoing convective instabilities.

Indeed, the similarities between vibrationally induced flow and other fluid-dynamic mechanisms has been the main driver for an appreciable (still ongoing in many cases) attempt to unify available information to general criteria. Relevant examples of this practice or tendency are existing books or treatises on the subject [1,2].

As an extensive treatment of such aspects would not fit the present Introduction, here we limit ourselves to recalling the striking analogies, which have been found in the ability of all these forces to produce a well-known "dichotomy" in fluid dynamics. This duality concerns the direction of the temperature gradient in relation to the considered force. Put simply, if the direction of steady gravity, vibrationally induced periodic accelerations, or the unit vector perpendicular the free interface (where surface tension is active) has a component perpendicular to the gradient of temperature, then the tendency to produce fluid motion is an "intrinsic property" of the considered fluid system (i.e., convection does not require any threshold to be exceeded or bifurcation to be enabled); vice versa, if they are parallel, then fluid motion is excited as a result of an instability of a state, which would otherwise remain in static (quiescent) and thermally diffusive conditions.

Notably, the drive to understand the phenomena behind the onset of fluid motion and related patterning behavior in vibrated systems and their relationships or affinities with other forms of convection has approached a sort of plateau over the past 50 years after the realization that, besides the influence of the direction of shaking, the modes of vibrational convection also display a great sensitivity to the related frequency. Indeed, this parameter represents an additional degree of freedom with respect to the magnitude of steady

---

gravity or the fixed (constant) value of the surface tension derivative in classical thermogravitational or thermocapillary flows. Together with the related amplitude, the frequency of vibrations contributes to determine the dynamic response of the fluid and two main regimes have been identified accordingly: one attained for small frequencies and large amplitude of the vibrations, where fluid motion follows in a more or less synchronous way the evolution in time of the related driving force (the acceleration induced by vibrations in this case), and another when frequency is large and amplitude is small, where a flow that is essentially "steady" in nature takes over. Owing to the apparently counterintuitive mismatch between the forcing (an acceleration varying periodically in time) and the fluid response (steady flow), the latter has been the subject of some additional investigations. These have clarified that the steady (or time-averaged) velocity component can be properly accounted for through a potential flow model theory (see, e.g., Refs. [1–3]).

Apart from supporting the early stages of research in this field through significant computational simplifications, in particular, the greatest merit of the potential theory approach resides in the insights it has delivered into the convection mechanisms under investigation. As an example, it has been clarified that for the case where the temperature gradient is perpendicular to vibrations, the typical time-averaged pattern consists of four steady rolls (the so-called quadrupolar state [4]), while this steady flow reduces to a degenerate condition with no flow at all in the situation where vibrations are parallel to the prevailing temperature gradient [2,5–7]. In the latter case, however, the patterning behavior of the instantaneous flow becomes very complex and displays several textural transitions in the space of parameters as the assumption of large frequency and the related potential flow theory cease to be valid [8–10].

Although all these achievements might support the idea that knowledge in this area is quite mature, unfortunately, current theories still lack a comprehensive picture to predict the flow behavior of such systems in conditions for which the fluid itself is "elastic," i.e., liquids are considered, which besides being viscous have the ability to retain shear stresses inside even if there are no gradients of velocity or the fluid is in a completely motionless state. Current knowledge is essentially limited (with a few exceptions) to Newtonian fluids. Viscoelastic fluids remain a grand challenge problem for the research community engaged in developing first-principles models and simulations, as their flow response is intertwined with some of math's deepest unsolved questions about the stability of certain equations [11–16].

Successful (available) efforts, however, have shown that the typical outcomes of fluid elasticity are the so-called overstability and solution multiplicity concepts. The first refers to the ability of elastic behaviors to cause a significant decrease in the threshold to be exceeded for the onset of convection (in the aforementioned "parallel" case, i.e., the situations in which the temperature gradient is parallel to steady gravity [17,18]). At the same time, it can render the transition from an initial quiescent condition to a convective state a Hopf (oscillatory) bifurcation (as opposed to the equivalent stationary bifurcation for a Newtonian fluid [19–21]). The companion concept of multiplicity relates to the

often-observed large number of solutions, which coexist in the space of phases, differ with respect to the basin of attraction, and can manifest at the same time on increasing certain parameters [22,23].

For vibrational flow, in particular, Boaro and Lappa [24–26] could show that overstability in three-dimensional liquid layers for the "parallel" case and relatively small frequencies is always associated with solutions reminiscent of the superlattice structures typical of the so-called "complex order" [27]. Such peculiar modes of convection are due to the coexistence of two distinct spatial scales, each displaying a different temporal dependence, driven by the interplay of the time-varying (stabilizing or destabilizing) acceleration induced by vibrations and the ability of the fluid to store and release elastic energy. The only available results for the companion "perpendicular" configuration are due to Boaro and Lappa [28], who, however, concentrated on a system as simple as a square cavity. Building on the intrinsic ability of this configuration to reveal the hidden symmetries of the different convective modes that can be excited in the space of parameters, they pointed out that, apart from expanding the set of possible solutions, elasticity can lead to complex dynamics driven by the competition between the propensity of polymer molecules to return to a relaxed position and the external vibrations that stretch and shrink them on a regular basis. The main outcome of such a competition is the existence of a nonmonotonic behavior in terms of flow amplitude as the ratio between the characteristic time of the vibrations and the relaxation time of the fluid is varied, which displays a fascinating similarity with the resonances and antiresonances typical of multicomponent mechanical structures [29,30]. As research up until this point for the parallel case has been limited to infinitely extended systems [24–26] and has not yet branched out to finite-size systems leaving a void within the physics surrounding it, an attempt is made here to bridge such a gap by considering the square cavity in the parallel case.

II. MATHEMATICAL MODEL

In line with the objective set at the end of the Introduction, a two-dimensional (2D) square cavity having lateral no-slip and adiabatic walls ($\partial T / \partial \mathbf{n}|_{\text{wall}} = \mathbf{0}$) and with a fixed difference of temperature between the top and bottom no-slip walls is considered. The related reference system and the boundary conditions are reported in Fig. 1. This figure also shows that the direction of the vibrations (as uniquely defined through the related unit vector $\hat{\mathbf{n}}$) is fixed and parallel to the temperature gradient ∇T ("parallel configuration").

Building on earlier efforts in this area [9,10,25,26,28, 31–36], here we model mechanical vibrations as a sinusoidal displacement in time, i.e.,

$$\mathbf{s}(t^*) = b \sin(\omega t^*)\hat{\mathbf{n}}, \tag{1}$$

where b is the vibration amplitude and ω is the related angular frequency ($\omega = 2\pi f$). Through simple mathematical developments (a second derivative with respect to time), the corresponding acceleration can be represented formally as

$$\mathbf{a}_\omega(t^*) = \boldsymbol{\gamma} \sin(\omega t^*), \tag{2}$$

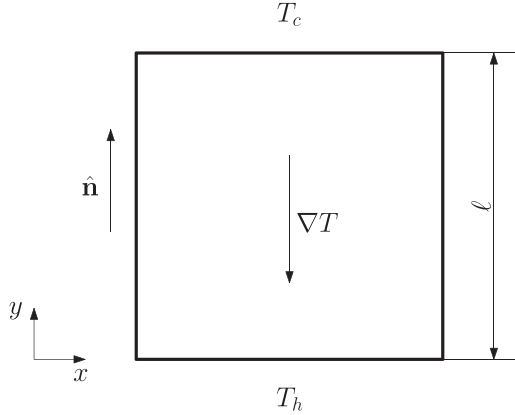where $\boldsymbol{\gamma} = -b\omega^2 \hat{\mathbf{n}}$.

FIG. 1. Sketch of the geometry and schematisation of the problem.

This is needed for the implementation of the Boussinesq approximation, namely the widespread practice of modeling the force term in the momentum balance equation as the product of the body acceleration affecting the fluid and a linear term accounting for the dependence of density on temperature, while the density is considered constant in all the other terms (valid for all liquids in particular and for all incompressible fluids more in general). In such a framework, the balance equations for mass, momentum, and energy in dimensional form read

$$\nabla \cdot \mathbf{u}^* = 0, \tag{3}$$

$$\rho \frac{\partial \mathbf{u}^*}{\partial t^*} + \rho \nabla \cdot (\mathbf{u}^*\mathbf{u}^*) = -\nabla p^* + \eta_s \nabla^2 \mathbf{u}^* + \nabla \cdot \tilde{\boldsymbol{\tau}}^*$$
$$+ \rho \beta_T (T - T_{\text{ref}}) \mathbf{a}_\omega(t^*), \tag{4}$$

$$\frac{\partial T^*}{\partial t^*} = -\nabla \cdot (\mathbf{u}^* T^*) + \alpha \nabla^2 T^*, \tag{5}$$

where t^* is the time, $\mathbf{u}^*$ is the velocity, T^* is the temperature, p^* is the pressure, $\tilde{\boldsymbol{\tau}}^*$ is the extra stress tensor due to the viscoelastic effect, ρ is the (constant) density of the fluid, η_s is the dynamic viscosity of the solvent (for Newtonian fluids $\eta_s = \eta$ simply represents the dynamic viscosity of the liquid), β_T is the thermal expansion coefficient (formally the proportional constant linking density and temperature), and α is the thermal diffusivity. The symbol (*) is used to highlight that the quantities are *dimensional*.

In addition to Eqs. (3), (4), and (5), an extra equation is needed to provide the required relationship between the viscoelastic stress tensor $\tilde{\boldsymbol{\tau}}^*$ and the velocity. It is therefore introduced separately. In particular, here, to allow direct comparison of the present results with those obtained previously for the companion "perpendicular configuration"[28], such equation is formulated according to the finitely extensible nonlinear elastic Chilcott-Rallison (FENE-CR) [37,38] paradigm.

In this regard, we wish to recall that, although the Oldroyd-B model is commonly employed for the analysis of the so-called Boger fluids (see, e.g., Refs. [20–22,24,39]), i.e., a class of viscoelastic liquids that maintain a constant viscosity over a wide range of shear rates [23], it is affected by a well-known problem, that is, it has an infinite extensional

viscosity. This is the reason for which we rely here on a more sophisticated variant where the linear (Hook) spring used for the derivation of the Oldroyd-B model is replaced by a finite extensible nonlinear one. In particular, the variant proposed by Chilcott and Rallison (FENE-CR) is the only FENE-type model that does not display shear-thinning or thickening behavior and therefore ideally suited to study the sole effect of viscoelasticity on the dynamics of interest.

The related equation for the temporal evolution of the extra stress tensor in its dimensional form reads

$$\lambda \left(\frac{\partial \tilde{\boldsymbol{\tau}}^*}{\partial t^*} + \mathbf{u}^* \cdot \nabla \tilde{\boldsymbol{\tau}}^* \right) + f(\text{tr}(\tilde{\boldsymbol{\tau}}^*))\tilde{\boldsymbol{\tau}}^*$$
$$= \eta_p f(\text{tr}(\tilde{\boldsymbol{\tau}}^*))[\nabla \mathbf{u}^* + (\nabla \mathbf{u}^*)^\mathsf{T}] + \lambda[\tilde{\boldsymbol{\tau}}^* \cdot \nabla \mathbf{u}^*$$
$$+ (\nabla \mathbf{u}^*)^\mathsf{T} \cdot \tilde{\boldsymbol{\tau}}^*], \tag{6}$$

where $f(\text{tr}(\tilde{\boldsymbol{\tau}}))$ is a quantity related to the possible deformation of the polymeric molecules:

$$f(\text{tr}(\tilde{\boldsymbol{\tau}}^*)) = \frac{L^2 + \dfrac{\lambda}{\eta_p}\text{tr}(\tilde{\boldsymbol{\tau}}^*)}{L^2 - 3}, \tag{7}$$

where η_p is the dynamic viscosity of the polymer, λ is the so-called *relaxation time*, and L^2 is the so-called *finite extensibility* parameter of the polymer molecule.

Other relevant physical parameters are the *total dynamic viscosity* of the viscoelastic fluid $\eta_0 = \eta_s + \eta_p$ and the *solvent-to-total* viscosity ratio $\xi = \eta_s/\eta_0$.

Equations (3), (4), (5), and (6) can be put in nondimensional form using the side ℓ of the square cavity as reference length, α/ℓ for the velocity, ℓ^2/α for the time, α/ℓ^2 for the frequency, $\rho\alpha^2/\ell^2$ for the pressure, $\Delta T = T_h - T_c$ for the temperature, and $\rho\nu_s\alpha/\ell^2$ for the extra stress tensor $\tilde{\boldsymbol{\tau}}^*$. In the last scaling factor ν_s is the kinematic viscosity of the Newtonian solvent ($\nu_s = \eta_s/\rho$).

Accordingly, the nondimensional balance equations in their time-dependent nonlinear form can be finally cast in compact form as

$$\nabla \cdot \mathbf{u} = 0, \tag{8}$$

$$\frac{\partial \mathbf{u}}{\partial t} = -\nabla p - \nabla \cdot (\mathbf{uu}) + \text{Pr}\nabla^2 \mathbf{u} + \text{Pr}\nabla \cdot \tilde{\boldsymbol{\tau}}$$
$$- \text{Pr}_g \text{Ra}_\omega T \sin(\Omega t)\hat{\mathbf{n}}, \tag{9}$$

$$\frac{\partial T}{\partial t} = -\nabla \cdot (\mathbf{u}T) + \nabla^2 T, \tag{10}$$

$$\vartheta \left(\frac{\partial \tilde{\boldsymbol{\tau}}}{\partial t} + \mathbf{u} \cdot \nabla \tilde{\boldsymbol{\tau}} \right) + f(\text{tr}(\tilde{\boldsymbol{\tau}}^*))\tilde{\boldsymbol{\tau}}$$
$$= \zeta f(\text{tr}(\tilde{\boldsymbol{\tau}}^*))[\nabla \mathbf{u} + (\nabla \mathbf{u})^\mathsf{T}] + \vartheta[\tilde{\boldsymbol{\tau}} \cdot \nabla \mathbf{u} + (\nabla \mathbf{u})^\mathsf{T} \cdot \tilde{\boldsymbol{\tau}}]. \tag{11}$$

The nondimensional groups that appear in these equations are the Prandtl number for the Newtonian solvent $\text{Pr} = \nu_s/\alpha$, the nondimensional frequency $\Omega = \ell^2\omega/\alpha$, the generalized Prandtl number $\text{Pr}_g = \text{Pr}/\xi$, the elasticity number $\vartheta = \lambda\alpha/\ell^2$, the viscosity ratio $\zeta = \eta_p/\eta_s = (1 - \xi)/\xi$, and the vibrational

Rayleigh number,

$$\mathrm{Ra}_\omega = \frac{b\omega^2\beta_T\Delta T\ell^3}{\nu_0\alpha}, \tag{12}$$

where $\nu_0 = \eta_0/\rho$ is the total kinematic viscosity. This expression can be seen as an alternate form of the classical Rayleigh number, where in place of the classical steady gravitational acceleration, the amplitude of the considered monochromatic periodic acceleration is used [28].

Following our preceding works [25,26,28], it is also worth introducing another parameter, that is, the ratio of the relaxation time λ (the characteristic time of the polymer molecules dynamics) and the period of the oscillations T_ω^* ($T_\omega = 2\pi/\Omega$, i.e., the characteristic time of the external dynamic force):

$$\Sigma = \frac{\lambda}{T_\omega^*} = \frac{\vartheta\Omega}{2\pi}. \tag{13}$$

The following expressions finally provide the definitions of three quantities, which we will use later to characterize the solutions provided by the numerical simulations, namely the Nusselt number $\mathrm{Nu}(t)$ (calculated on the heated boundary), the global Kinematic energy $K(t)$, and the global elastic energy $\mathrm{EE}(t)$,

$$\mathrm{Nu}(t) = \frac{1}{A}\int_A \nabla T(t)\cdot\mathbf{n}_{\mathrm{plate}}\,dA, \tag{14}$$

$$K(t) = \frac{1}{V}\int_V \mathbf{u}\cdot\mathbf{u}\,dV, \tag{15}$$

$$\mathrm{EE}(t) = \frac{1}{V}\int_V \mathrm{tr}(\tilde{\boldsymbol{\tau}})\,dV, \tag{16}$$

where $\mathbf{n}_{\mathrm{plate}}$ in the unit vector normal to the boundary and A is the area of the heated boundary, V is the volume of the cavity, and $\mathrm{tr}(\tilde{\boldsymbol{\tau}})$ is a quantity proportional to the elastic energy stored by the polymer molecules (see Ref. [25] and references therein). In addition to the instantaneous values of the three quantities defined above, it is common practice to define their time average counterpart $\overline{\mathrm{Nu}}$, $\overline{K}$, and $\overline{\mathrm{EE}}$ as

$$\overline{\mathrm{Nu}} = \frac{1}{T_{\mathrm{Nu}}}\int_{T_{\mathrm{Nu}}}\mathrm{Nu}(t)\,dt, \tag{17}$$

$$\overline{K} = \frac{1}{T_K}\int_{T_K}K(t)\,dt, \tag{18}$$

$$\overline{\mathrm{EE}} = \frac{1}{T_{\mathrm{EE}}}\int_{T_{\mathrm{EE}}}\mathrm{EE}(t)\,dt, \tag{19}$$

where T_{Nu}, T_K, and T_{EE} are the oscillation period of Nusselt number, global kinematic, and elastic energy, respectively.

III. NUMERICAL METHOD

The balance equations (3), (4), (5), and (6) are solved in the framework of a segregated finite-volume method (in space and time) using the computational platform OpenFOAM. This time-marching algorithm is a well-known numerical realization of the PISO method originally elaborated by Issa [40] (see also Refs. [41,42]), with a collocated disposition for the primitive variables and the Rhie and Chow [43] interpolation scheme exploited to avoid pressure-velocity coupling problems [23].

Moreover, for the implementation of the viscoelastic model, we have used rheoTool [44], a versatile instrument to tackle problems involving complex fluids [45–47], relying on a set of strategies by which the numerical integration process of the viscoelastic stress transport equation can be made more stable (thereby allowing exploration of a wider region of the space of parameters). The advantages of this approach with respect to the one implemented in our earlier works (the both sides diffusion technique [25,26,28]) resides in its log-conformation tensor nature [45,48], which gives it the aforementioned improved stability properties and, at the same time, makes it more accurate in capturing flow instabilities. With the log-conformation approach the viscoelastic stress tensor $\tilde{\boldsymbol{\tau}}$ is expressed as a function of the conformation tensor $\mathbf{A}$, i.e., a quantity proportional to the level of deformation of the polymer molecules [49]. In particular, for a FENE-CR fluid, the relationship between the two tensors reads [50]:

$$\tilde{\boldsymbol{\tau}}^* = \frac{\eta_p\tilde{f}}{\lambda}(\mathbf{A}-\mathbf{I}), \tag{20}$$

where $\mathbf{I}$ is the unit tensor and $\tilde{f} = L^2/[L^2 - \mathrm{tr}(\mathbf{A})]$.

In general, the conformation tensor is a positive definite quantity; however, in proximity to a critical point (a "singularity" due to the hyperbolic nature of the viscoelastic stress transport equation, see Refs. [11–15]) the positiveness of $\mathbf{A}$ can drop thereby leading to divergence of the numerical procedure. If, instead of considering $\mathbf{A}$, its natural logarithm is used, then $\boldsymbol{\Theta} = \ln(\mathbf{A})$ can remain definite positive and, accordingly, the aforementioned singularity-related problem can be strongly mitigated. Rewriting and solving (6) in terms of $\boldsymbol{\Theta}$, rheoTool calculates the value of the stress tensor using an exponential transformation and Eq. (20) (Ref. [45] and references therein).

Moreover, we have used a second-order accurate backward scheme to discretize the equations in time, a second-order accurate central difference scheme for the spatial discretization of the diffusive terms and a third-order CUBISTA scheme for the analogous treatment of the convective terms. To avoid nonphysical oscillations, the CUBISTA scheme is implemented through a deferred correction approach and the nonscalar quantities are handled in a component-wise way [45].

This approach has been validated in other works of the present authors for thermogravitational, thermovibrational, and thermocapillary flows. The reader is referred to Refs. [23,25,28,51] for a complete treatment of the topic.

Mesh refinement study

A representative case for the mesh refinement analysis is selected as follows. The Prandtl number and viscosity ratio are set to $\mathrm{Pr}_g = 10$ and $\xi = 0.5$, respectively (as these are the fixed dimensionless values considered in this study); moreover, in line with the conditions considered in the results section, $\Omega = 100$ (maximum value of angular frequency), $\mathrm{Ra}_\omega = 2.8\times10^4$ (close to the maximum value of the vibrational Rayleigh number), and $\vartheta = 0.1$ (value located in the center of the range explored in this study). The corresponding variations of $\overline{\mathrm{Nu}}$, $\overline{K}$, and $\overline{\mathrm{EE}}$ on varying the mesh size are reported in Table I. As quantitatively substantiated in this table, an increase in numerical resolution from a mesh 80×80

TABLE I. Mesh refinement study; case $\mathrm{Pr}_g = 10$, $\xi = 0.5$, $\Omega = 100$, $\mathrm{Ra}_\omega = 2.8 \times 10^4$, and $\vartheta = 0.1$.

Mesh size	$\overline{\mathrm{Nu}}$	$\overline{K}$	$\overline{\mathrm{EE}}$	%err $\overline{\mathrm{Nu}}$	%err $\overline{K}$	%err $\overline{\mathrm{EE}}$
20×20	1.60	294.6	36.6			
40×40	1.79	724.0	91.9	11.88	145.76	151.09
60×60	2.014	948.0	138.0	12.51	30.94	50.16
80×80	2.04	1001	149.2	1.29	5.59	8.12
100×100	2.04	1032	155	0	3.1	3.89

to 100×100 does not produce appreciable changes in the Nusselt number. The corresponding variations of kinetic and elastic energy are less than 4%, which is an acceptable compromise between accuracy ad time consumption. For these reasons, a mesh having 80 divisions along the vertical and horizontal side of the cavity is chosen for the analysis presented in Sec. IV.

IV. RESULTS

As even a cursory glimpse into the earlier section would immediately confirm, the considered problem is characterized by a rich set of influential parameters, which lead naturally to the need of a reasonable choice about those which have to be fixed and those to be varied (not to make the scale of the overall problem intractable). For consistency with Boaro and Lappa [28], here, in particular, Pr_g and ξ are fixed to $\mathrm{Pr}_g = 10$ and $\xi = 0.5$, respectively. The angular frequency and vibrational Rayleigh number, however, are allowed to span relatively wide ranges, namely $\Omega = 25, 50, 75,$ and 100 and $\mathrm{Ra}_\omega \in [\mathrm{Ra}_{\omega,\mathrm{cr}}, 3.3 \times 10^4]$, where $\mathrm{Ra}_{\omega,\mathrm{cr}}$ is the critical vibrational Rayleigh number for the onset of thermovibrational convection. Moreover, different values of the elasticity number, $\vartheta = 0.10, 0.15,$ and 0.20, are examined.

An experimentalist may determine relevant physical conditions corresponding to all these nondimensional factors in a relatively straightforward way. The considered fluids (for which the FENE-CR paradigm is applicable) are indeed the so-called Boger fluids, i.e., water-based polymer dilute solutions at ambient or moderate temperatures, e.g., water between 25°C and 50°C with limited amount of a polymer such a PAM, PEG, PEO, PVP, xanthan gum, etc.

The Prandtl number of these liquids is very similar to that considered in the present work (in this regard, we wish also to highlight that the rheological characteristic ratios Pr_g and ξ used here are almost identical to those examined by Li and Khayat [21]). By assuming $\lambda \approx 10^{-2}\,\mathrm{s}$ (typical realistic value for a relatively small polymer concentration) and $\alpha \approx 1.44 \times 10^{-7}\,\mathrm{m^2/s}$ (e.g., for a water solution at 35°C), the corresponding characteristic cavity size, obtained by substituting these values into the expression of the elasticity number (e.g., $\vartheta = 0.15$), would read $\ell \approx 10^{-4}\,\mathrm{m}$ (microfluidics conditions). The dimensional frequency of the vibrations can be determined accordingly using the expression of the nondimensional angular frequency, e.g., for $\Omega = 100$, $\omega = \Omega\alpha/\ell^2 \approx 1.4 \times 10^3\,\mathrm{rad/s}\,(\rightarrow\ f \approx 2 \times 10^2\,\mathrm{Hz})$. The required ΔT finally stems from the definition of the Rayleigh number. Using $\mathrm{Ra}_\omega = 10^4$ as a representative condition and solvent kinematic
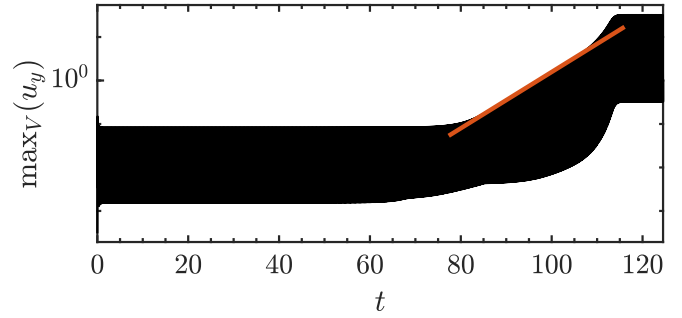

FIG. 2. Evolution in time of the vertical velocity maximum for the case of $\Omega = 50$, $\vartheta = 0.15$, and $\mathrm{Ra}_\omega = 8.89 \times 10^3$. Amplifying disturbances. The angular coefficient of the orange line represents the disturbance growth rate.

viscosity and thermal expansion coefficient (at 35°C) $\eta_s = 0.72 \times 10^{-6}\,\mathrm{m^2/s}$ and $\beta_T = 4 \times 10^{-4}\,\mathrm{K^{-1}}$, respectively, this would lead to a $\Delta T \cong 75°\mathrm{C}$ for a vibration amplitude of a few centimeters ($b \cong 3 \times 10^{-2}\,\mathrm{m}$).

A. Neutral curves

According to the principles of the classical linear stability analysis (LSA), the basic (equilibrium) state of a dynamic system becomes (locally) unstable against a certain class of infinitesimal disturbances only if the set of parameters describing the system belongs to a region of the space of parameters where such disturbances can be amplified. Such amplification is mathematically represented (in the framework of the LSA approach) by an exponential behavior, which, in turn can be directly put in relation with the eigenvalues of the Jacobian of the linearized equations [19].

Although the present approach does not rely on LSA, the above concepts still represent a useful basis on which the (critical) conditions for the onset of convection can be determined. Indeed, the required theoretical link is provided by the realization that the numerical approach described in the earlier section can provide information directly on the amplitude of disturbances and the related evolution in time. Backward extrapolation (to zero) of the disturbance growth rate on a semilogarithm scale can be used to determine the same value of the critical parameter, which would be provided in principle by the LSA.

Using a diffusive state (linear distribution of the temperature in y direction and stationary fluid) as an initial condition and monitoring the global maximum of the y component of the velocity over time [$\max_V(u_y)$, where V is the volume of the domain] it is easy to assess whether the disturbance is amplifying. Specifically, since from LSA it is known that the disturbance will grow exponentially at the onset of convection, the best way to do so is to plot $\max_V(u_y)$ in a semilogarithmic plane (y axis having a logarithmic scale). In Fig. 2 we report an example of an amplifying disturbance.

It is worth highlighting that the oscillations of the velocity maximum present in such a figure between $t = 0$ and $t \approx 80$ with average value $\approx 10^{-2}$ represent "numerical noise" preceding the stage in which these "random" disturbances are amplified through the aforementioned exponential growth process (until their amplitude is saturated and the related

TABLE II. Critical values of the vibrational Rayleigh number $Ra_{\omega,cr}$ as a function of the elasticity number and angular frequency. Case $Pr_g = 10$, $\xi = 0.5$.

			ϑ	
		0.1	0.15	0.2
Ω	25	5358	4545	4292
	50	9280	8853	9023
	75	14 061	14 785	15 634
	100	20 432	22 087	23 563

average value attains a value as high as 10, i.e., three orders of magnitude larger than that of the initial disturbances). The physical mechanism driving the amplification of the disturbances is the same envisaged by the LSA approach. The difference with respect to the LSA is represented by the fact that, while with LSA the disturbances "must be added" to the initial "basic solution" in the form of mathematical functions of given shape (with some initial guesses on the wave number which is thought to be the most critical), when the problem is addressed through direct numerical solution of the governing time-dependent and nonlinear equations (present case) small-scale disturbances are naturally produced by the simulation in the form of numerical noise. Only the components of such a wideband noise with the "right" wave number are selected out of the full spectrum of disturbances and amplified accordingly. This approach has already enjoyed a widespread use in the literature and it is the main reason for which any numerical simulation of a very classical phenomenon such as standard Rayleigh-Bénard convection can capture this form of convection even if no disturbances are artificially superimposed on the initial quiescent state (see, e.g., Ouertatani *et al.* [52] and Stella and Bucchignani [53] and references therein).

The orange line inclination (angular coefficient) represents the *growth rate* (ε) of the instability. To calculate the critical value of the vibrational Rayleigh number, it is sufficient to estimate the law $\varepsilon(Ra_\omega)$ in a region close to the critical threshold. The critical value of the vibrational Rayleigh number ($Ra_{\omega,cr}$) is recovered by extrapolating ε to 0. The outcomes of this process are reported in Table II, where $Ra_{\omega,cr}$ is given as a function of the couple (ϑ, Ω).

Figure 3 provides additional insights into such dependencies by showing separately the effects of ϑ and Ω. In particular, Fig. 3(a) makes evident that, in general, lower frequencies are more destabilizing than the higher ones. This result is in accordance with other studies involving Newtonian [8,9] fluids. Indeed, in the limit $\Omega \to 0$ the thermovibrational flow tends to the standard thermogravitational counterpart, i.e., case where the acceleration has never a stabilizing role (in the vibrational case, the acceleration tends to kill the flow in the part of the period where it is directed from the hot to the cold wall); vice versa, when Ω attains a high value, there is an increase in the critical threshold (which would theoretically become infinite in the limit as $\Omega \to \infty$, i.e., when the flow enters the aforementioned potential flow regime).

Although the concept of overstability discussed by Boaro and Lappa [25] is still valid in the present case (as an example we could verify that no convection is produced in an
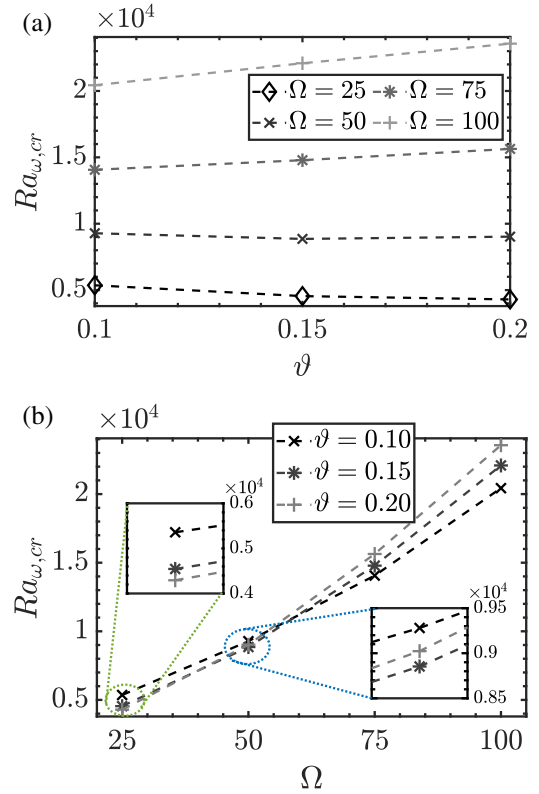

FIG. 3. Influence of ϑ (a) and Ω (b) on the critical vibrational Rayleigh number.

equivalent Newtonian fluid with $Pr = 10$ subjected to vibrations with $\Omega = 100$ although a value of the Rayleigh number as high as $Ra_\omega = 2.5 \times 10^4$ is considered), providing a clear picture about the effect of the elasticity number is less straightforward.

A destabilizing trend has been found for this specific value of the angular frequency ($\Omega = 25$), which essentially confirms the earlier conclusions by Boaro and Lappa [25] (although those results were obtained for the case of the infinite layer and different conditions: $Pr_g = 7$, $\Omega = 26.5$, $\xi = 0.1$). Like in that study, here the critical Rayleigh number decreases monotonically as the elasticity number is increased if relatively small values of the angular frequency are considered. This result is also in accordance with the classic literature about Rayleigh-Bénard (RB) convection in viscoelastic fluid [20,21].

Extension of the investigated range of angular frequencies to much larger values (up to $\Omega = 10^2$, main objective of the present work) has revealed that this trend can be reversed. In particular, the inversion seems to occur for $\Omega \approx 50$ for which the critical Rayleigh number remains almost constant over the considered ϑ interval while displaying a barely appreciable nonmonotonic dependence [see Fig. 3(b)]. For larger values of Ω, however, a completely different scenario emerges, with an increase in elasticity producing flow stabilization rather than "overstability" (the critical threshold increases with ϑ), which is the opposite of what one would expect in standard RB viscoelastic convection.

TABLE III. Different values of Σ as a function of ϑ and Ω.

		ϑ		
		0.1	0.15	0.2
Ω	25	0.40	0.60	0.80
	50	0.80	1.19	1.59
	75	1.19	1.79	2.38
	100	1.59	2.39	3.18

Notably, this scenario is reminiscent of that reported by Boaro and Lappa [28] (see Figs. 20 and 21 in their work), for the square cavity with vibrations "perpendicular" to the temperature gradient. As already explained to a certain extent in the Introduction, they found that, in analogy with the behavior of certain multicomponent mechanical systems that undergo resonances and antiresonances, vibrated viscoelastic systems can also display regions of variable stability. More precisely, they observed that for values of the parameter Σ smaller than one, where Σ is the ratio between relaxation time and period of the forcing vibrations as formally defined in Eq. (13), the intensities of the mean and instantaneous viscoelastic stress tensor components increase with Σ, whereas for $\Sigma > 1$ they are inversely proportional to ϑ (and therefore Σ).

The corresponding variation of the parameter Σ for the conditions considered in the present work can be gathered from Table III, where it is reported as a function of ϑ and Ω. It can be seen there that for $\Omega = 50$, Σ varies in a relatively restricted neighborhood of 1, which confirms that the nonmonotonic evolution laws or dependencies are not an exclusive prerogative of the perpendicular case. Just like variations of Σ in a narrow range around to the value of 1 can cause nonmonotonic changes in the flow amplitude in the case with vibrations perpendicular to the temperature gradient, it can produce similar variations in the critical threshold for the onset of convection in the parallel case.

As illustrated further in the next section, changing the vibrational frequency can also impact significantly the patterning behavior (for brevity, we limit ourselves to considering the cases $\Omega = 50, 75,$ and 100 for which the interesting behaviors reported above have been obtained).

B. Pattern selection and observed bifurcations

The simplest way to elaborate a relevant classification of the emerging patterns in terms of symmetries and multiplicity of the related cellular structure is to rely on the approach originally implemented by Mizushima [54], where the set of possible modes of convection in a square cavity was partitioned into four fundamental classes (see Fig. 4), namely

(aa): The antisymmetric-antisymmetric mode, where both the x and y symmetry are lost as a result a flow structure featuring an odd number of rolls along both directions.

(sa): The symmetric-antisymmetric mode, where only the symmetry with respect to the (vertical) y axis is retained by virtue of an even number of rolls along the x direction (and an odd number of rolls along y).

(as): The antisymmetric-symmetric mode, where only the symmetry with respect to the (horizontal) x axis is retained by
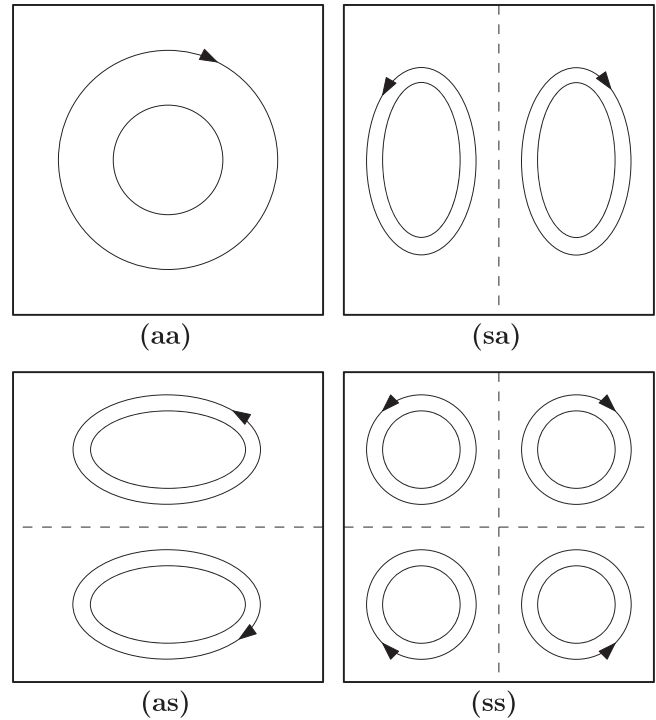

FIG. 4. Categorization of possible solutions of buoyancy convection in 2D finite enclosures in terms of related symmetries.

virtue of an even number of rolls along y (and an odd number of rolls along the x).

(ss): The symmetric-symmetric mode, where both symmetries are preserved by virtue of an even number of vortex cells along both the x and y axes, this leading to a centrosymmetric configuration when the number of rolls along both the x and y directions is the same and to a columnar arrangement if the number of rolls along y is larger.

For the considered problem, we have found two dominant symmetries, namely the (aa) and (sa). Additional insights into these modes of convection can be gathered from Fig. 5, which quantitatively substantiates the relationship between the considered value of the vibrational Rayleigh number $\mathrm{Ra}_\omega \in [\mathrm{Ra}_{\omega,\mathrm{cr}}, 3.3 \times 10^4]$ and the "global measures" defined in Sec. II, i.e., $\overline{\mathrm{Nu}}$, $\overline{K}$, and $\overline{\mathrm{EE}}$.

Following up on the previous point, the first column of Fig. 5 provides a first glimpse of the effect of the vibrational Rayleigh number on $\overline{\mathrm{Nu}}$. It can be seen that while for $\Omega = 50$ the time average Nusselt number increases with a concave down parabolic law at the onset of convection, for $\Omega = 75$ and 100 the curve is concave upwards. Similar considerations can be made for the $\overline{K}$ and $\overline{\mathrm{EE}}$ graphs. This difference is due to the fact that at $\Omega = 50$ the flow emerging from the diffusive state displays an (aa) symmetry. On the contrary, for the other two values of the angular frequency, the dominant symmetry is the (sa).

For $\Omega = 50$ the (aa) configuration is stable in the range $\mathrm{Ra}_{\omega,\mathrm{cr}} \leqslant \mathrm{Ra}_\omega \leqslant 1.575 \times 10^4$ for $\vartheta = 0.10$, $\mathrm{Ra}_{\omega,\mathrm{cr}} \leqslant \mathrm{Ra}_\omega \leqslant 1.525 \times 10^4$ for $\vartheta = 0.15$, and $\mathrm{Ra}_{\omega,\mathrm{cr}} \leqslant \mathrm{Ra}_\omega \leqslant 1.525 \times 10^4$ for $\vartheta = 0.20$.

Instead, for $\Omega = 75$ the (sa) configuration is stable in the range $\mathrm{Ra}_{\omega,\mathrm{cr}} \leqslant \mathrm{Ra}_\omega \leqslant 1.515 \times 10^4$ for $\vartheta = 0.10$,
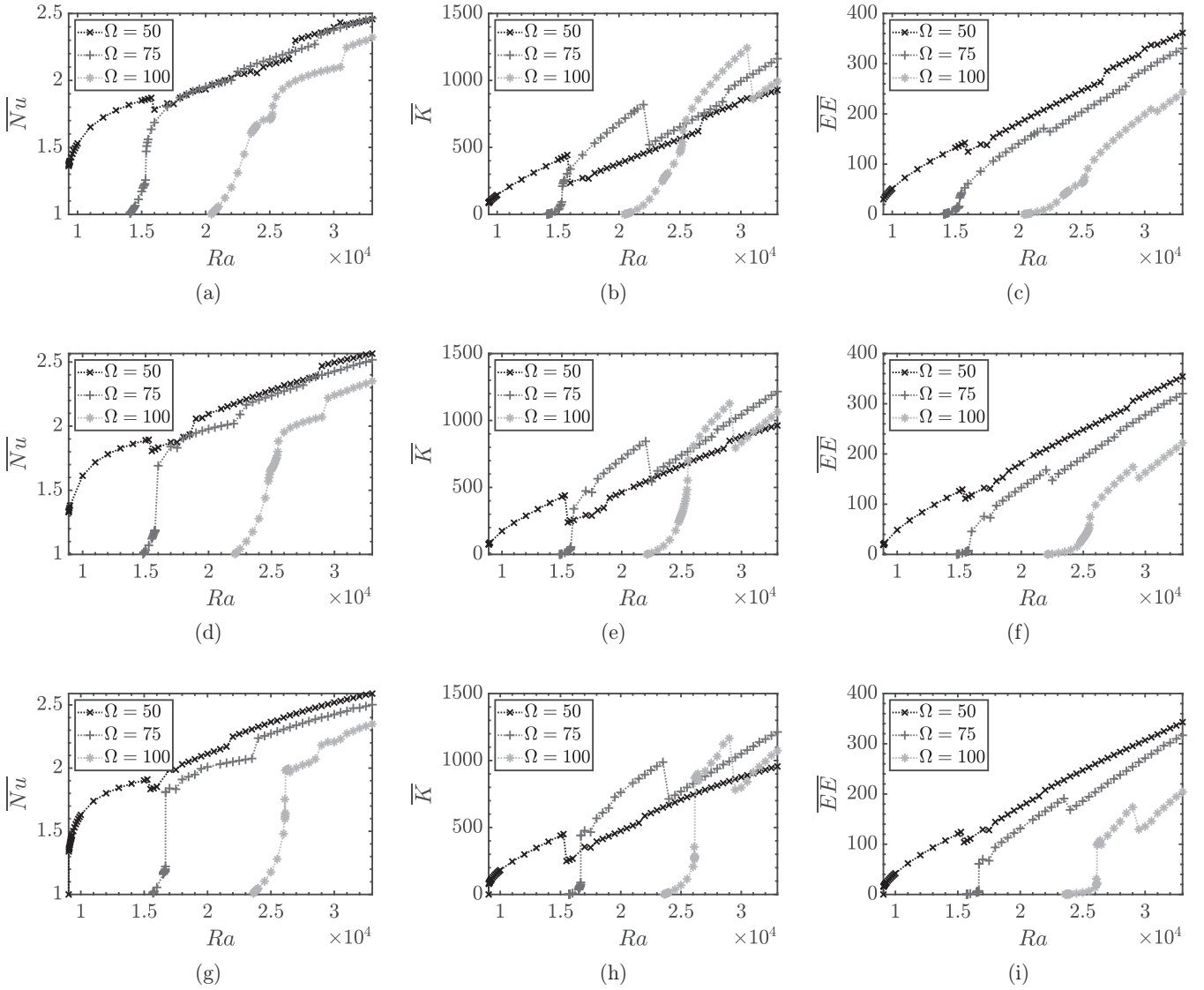
FIG. 5. Variation of $\overline{\mathrm{Nu}}$ (first column), $\overline{K}$ (second column), and $\overline{\mathrm{EE}}$ (third column) for $\vartheta = 0.10$ [(a)–(c)], $\vartheta = 0.15$ [(d)–(f)], and $\vartheta = 0.20$ [(g)–(i)] as a function of the vibrational vibrational Rayleigh number.

$\mathrm{Ra}_{\omega,\mathrm{cr}} \leqslant \mathrm{Ra}_\omega \leqslant 1.571 \times 10^4$ for $\vartheta = 0.15$ and $\mathrm{Ra}_{\omega,\mathrm{cr}} \leqslant \mathrm{Ra}_\omega \leqslant 1.652 \times 10^4$ for $\vartheta = 0.20$ while for $\Omega = 100$ the corresponding intervals are $\mathrm{Ra}_{\omega,\mathrm{cr}} \leqslant \mathrm{Ra}_\omega \leqslant 2.630 \times 10^4$ for $\vartheta = 0.10$, $\mathrm{Ra}_{\omega,\mathrm{cr}} \leqslant \mathrm{Ra}_\omega \leqslant 2.490 \times 10^4$ for $\vartheta = 0.15$, and $\mathrm{Ra}_{\omega,\mathrm{cr}} \leqslant \mathrm{Ra}_\omega \leqslant 2.6148 \times 10^4$ for $\vartheta = 0.20$.

By denoting by Ra_ω^I the right end of such a stability interval, Fig. 5 is also instrumental in showing that on exceeding Ra_ω^I, a second bifurcation takes place. For $\Omega = 50$, the (aa) dominated solution is taken over by a (sa) symmetric configuration, and vice versa, the (sa) configuration becomes an (aa) flow when $\Omega = 75$ and 100. The sudden change in the solution comes with an abrupt variation of $\overline{\mathrm{Nu}}$, $\overline{K}$, and $\overline{\mathrm{EE}}$. In particular, on jumping from an (aa) to a (sa) solution all these three quantities are lowered, whereas they abruptly increase when going from a (sa) to an (aa) branch (it is worth recalling here that similar phenomena have been observed in other categories of viscoelastic flows, e.g., the transition from traveling-wave to standing-wave solutions reported by Lappa

and Boaro [23] for RB flow in cylindrical configurations with lateral stress-free conditions).

For $\Omega = 50$ the (sa) configuration is stable in the range $\mathrm{Ra}_\omega^I < \mathrm{Ra}_\omega \leqslant 3.3 \times 10^4$ for $\vartheta = 0.10, 0.15$, and 0.20. Therefore, in this case, the flow maintains the (sa) configuration over a relatively wide range of vibrational Rayleigh numbers.

An increase in the frequency makes the system response more involved. While for $\Omega = 75$ and $\vartheta = 0.15$, and $\Omega = 100$ and $\vartheta = 0.20$, the flow bifurcates directly from the (sa) to (aa) mode of convection when $\mathrm{Ra}_\omega > \mathrm{Ra}_\omega^I$; for all the other cases there is a range of the control parameter for which the flow displays an *intermittent* response. These solutions will be analyzed in detail in Sec. IV C.

To summarize, for $\Omega = 75$ the (aa) symmetry stability range is $1.535 \times 10^4 \leqslant \mathrm{Ra}_\omega \leqslant 2.2 \times 10^4$ for $\vartheta = 0.10$, $\mathrm{Ra}_\omega^I < \mathrm{Ra}_\omega << 2.2 \times 10^4$ for $\vartheta = 0.15$, and $1.669 \times 10^4 \leqslant \mathrm{Ra}_\omega \leqslant 2.35 \times 10^4$ for $\vartheta = 0.20$ while for $\Omega = 100$ the range is $2.525 \times 10^4 \leqslant \mathrm{Ra}_\omega \leqslant 3.05 \times 10^4$ for $\vartheta = 0.10$, $2.555 \times$
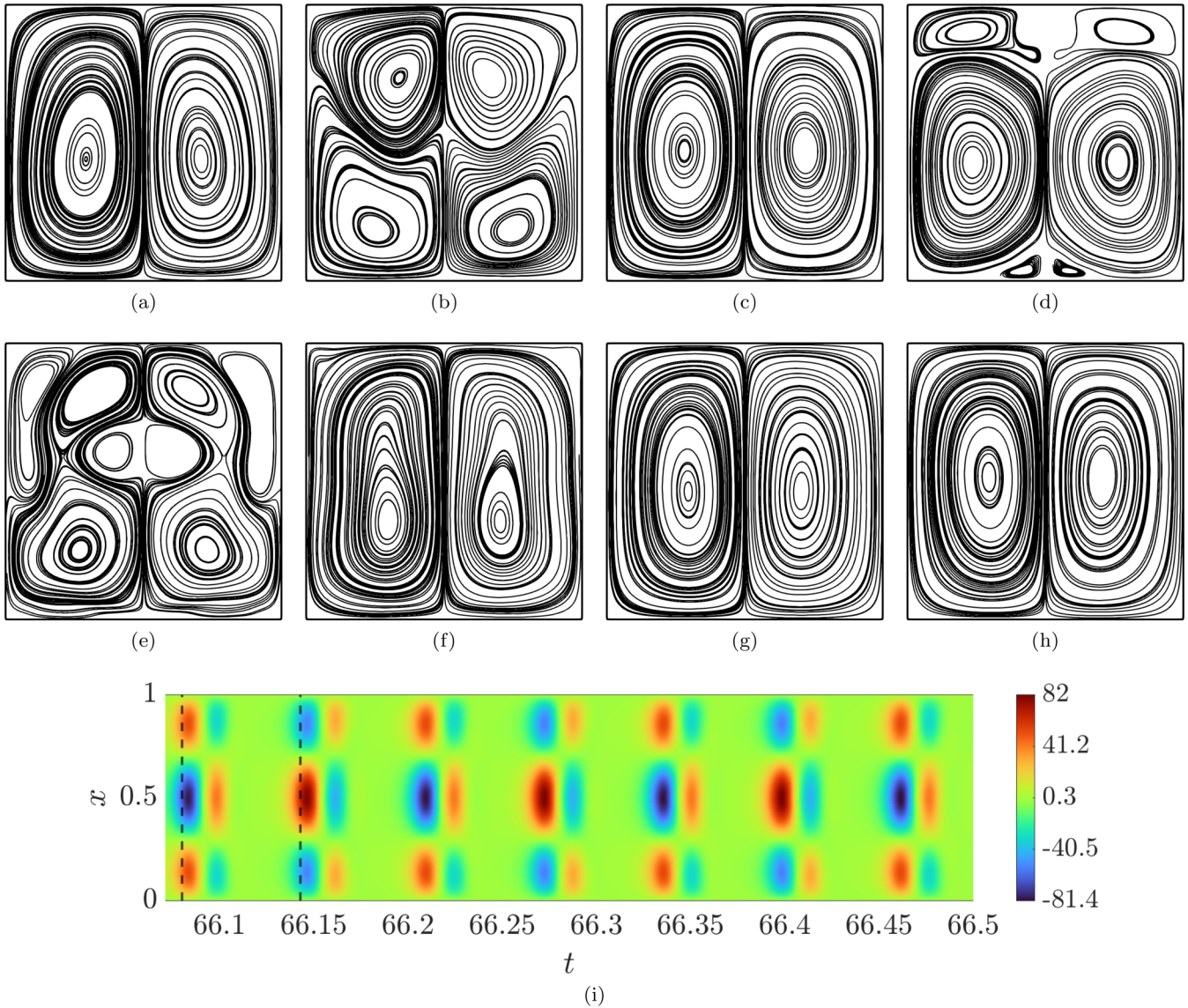
FIG. 6. Pattern evolution for the case of $Pr_g = 10$, $\xi = 0.5$, $\vartheta = 0.10$, $\Omega = 100$, and $Ra_\omega = 2.355 \times 10^4$. The streamlines are sampled evenly over a period of the external vibration (half a period of the pattern dynamic evolution) [(a)–(h)]. The spatiotemporal map (i) represent the vertical component of the velocity (u_y) over the center-line orthogonal to the side-walls ($0 \leqslant x \leqslant 1$ and $y = 0.5$). The vertical dotted lines show the interval over where the streamlines where sampled starting at $t_0 = 66.08$. Cavity heated from below.

$10^4 \leqslant Ra_\omega \leqslant 2.9 \times 10^4$ for $\vartheta = 0.15$, and $Ra_\omega^I < Ra_\omega$ $\leqslant 2.9 \times 10^4$ for $\vartheta = 0.20$.

By indicating with Ra_ω^{II} the next bifurcation point for the (aa) symmetry stability interval related to the $\Omega = 75$ and $\Omega = 100$ branches, the symmetry of the system changes again as soon as it is exceeded, returning to a (sa) configuration. For all the considered solutions, this symmetry is stable in the interval $Ra_\omega^{II} < Ra_\omega < 3.3 \times 10^4$.

At this stage, we also wish to highlight that, in analogy to thermovibrational convection in an infinite layer of viscoelastic fluid [25,26], the temporal response of the system to the application of vibrations in all these cases has found to be subharmonic, i.e., the flow evolves in time with a frequency that is half of the forcing frequency. The related patterning behavior is depicted for two representative cases, i.e., $\Omega = 100$, $\vartheta = 0.10$, and $Ra = 2.355 \times 10^4$ for the (sa) symmetry and

$Ra = 2.55 \times 10^4$ for the (aa) symmetry in Fig. 6 and Fig. 7, respectively. For both cases, the related spatiotemporal map of the vertical component of the velocity (u_y) over a horizontal line passing through the center of the cavity ($0 \leqslant x \leqslant 1$, $y = 0.5$) is also reported. The dashed vertical lines in the maps represent the time interval where the streamlines were sampled. These maps are a useful tool to represent in a compact way the system dynamic evolution [10,25,26].

A detailed interpretation of the phenomena shown in these figures can be provided as follows. For the (sa) case reported in Fig. 6, at the beginning of the oscillation period [Fig. 6(a)] the flow displays the typical two counter-rotating cells (compare with Fig. 4), which occupy the whole available space and the convective cell on the left (right) rotates clockwise (anticlockwise). The sense of rotation can be directly inferred from the spatiotemporal map [Fig. 6(i)]. As the time progresses,
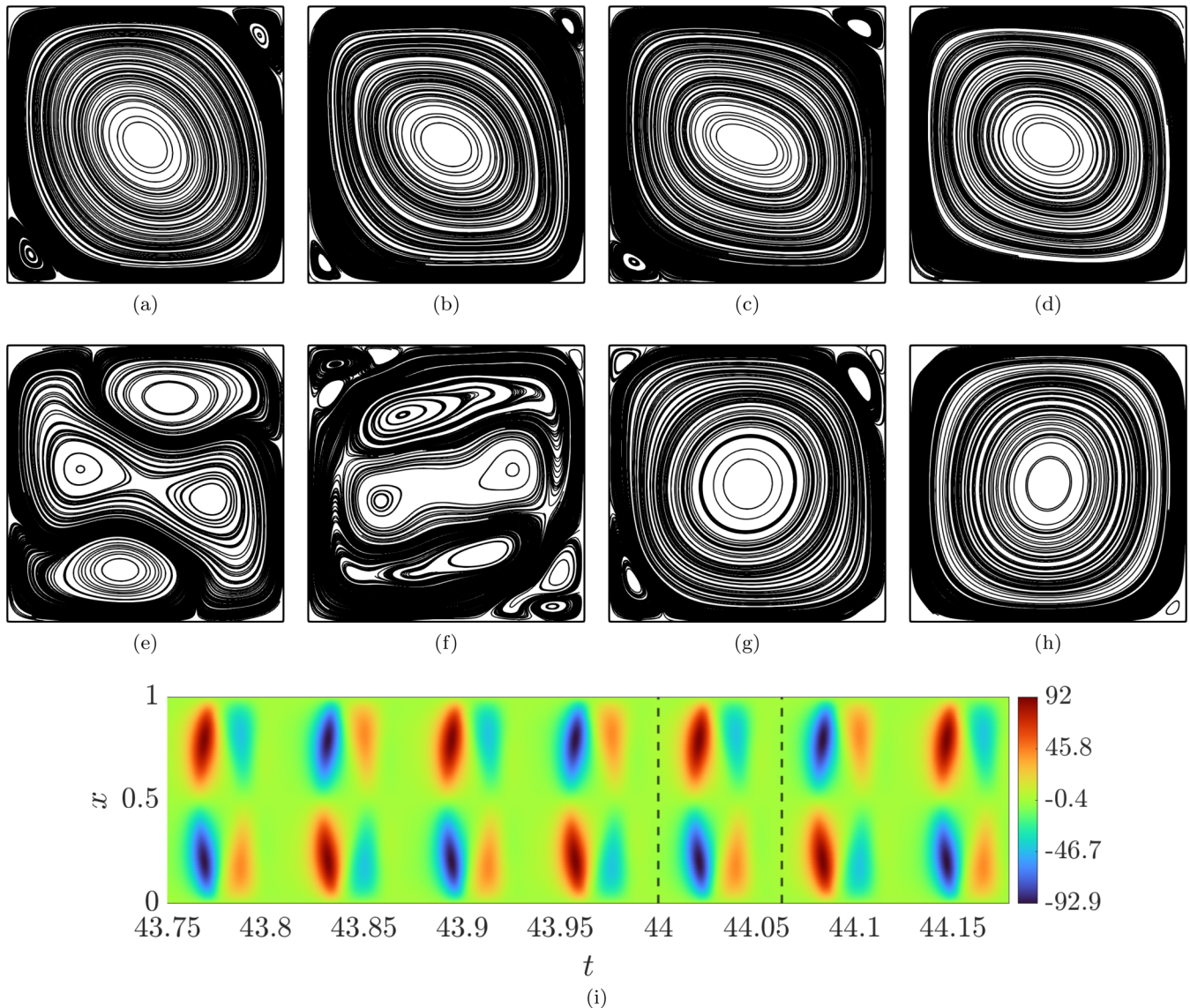
FIG. 7. Pattern evolution for the case of $Pr_g = 10$, $\xi = 0.5$, $\vartheta = 0.10$, $\Omega = 100$, and $Ra_\omega = 2.55 \times 10^4$. The streamlines are sampled evenly over a period of the external vibration (half a period of the pattern dynamic evolution) [(a)–(h)]. The spatiotemporal map (i) represent the vertical component of the velocity (u_y) over the center-line orthogonal to the side-walls ($0 \leqslant x \leqslant 1$ and $y = 0.5$). The vertical dotted lines show the interval over where the streamlines where sampled starting at $t_0 = 44$. Cavity heated from below.

two small cells, rotating in the opposite direction with respect to the initial ones, nucleate in proximity to the cold boundary [Fig. 6(b)] and grow until their size becomes comparable to the cavity height, thereby suppressing the two initial cells [Fig. 6(c)]. The associated map is instrumental in showing that the new cells rotate in the opposite direction. In the meantime, the external vibrations have entered their "stabilizing" period, as confirmed in the map by the sudden decrease in the velocity intensity [Figs. 6(d) and 6(i)]. However, the system never attains a motionless state (this is one of the main differences from studies dealing with Newtonian fluids [9,10]). Rather, by leveraging the elasticity accumulated in the fluid (i.e., the energy that was stored in the polymer molecules during the destabilizing phase), the system is able to maintain the ongoing unsteady flow. This conclusion is supported by both the spatiotemporal map and the analysis of Nu, K, or EE signals (omitted for the sake of brevity). Between frames 6(e)

and 6(h) there are two other inversions until, at the end of the period of vibrations, the (sa) is recovered. However, the sense of rotation is not the same as the initial one. This is the manifestation of the aforementioned half-subharmonicity of the spatiotemporal behavior. As evident from the map, before recovering the initial situation another period of vibrations is needed. During the second period, the evolution is mirror-symmetric with respect to the one just analyzed (for the sake of brevity, the description of the pattern evolution over the second period is omitted).

Similar considerations can be made for the evolution of the pattern with (aa) symmetry. Starting from the initial situation depicted in Fig. 7(a), a single cell occupying almost the whole volume of the cavity and rotating anticlockwise can be seen. Smaller eddies are located in the northeast and southwest corners. As time passes, the size of these two eddies oscillates, as visible in Figs. 7(b)–7(d) until at a certain stage they start

growing [Fig. 7(e)], thereby compressing the main central cell and merging with it [Fig. 7(f)]. As a result, another central patch of fluid rotating clockwise is formed Fig. 7(g). In the meantime, the direction of the vibrations has become stabilizing for the flow. However, since the intensity of convection is now stronger [Fig. 5(a)], this indirectly confirms that the fluid has stored more energy with respect the previous case [see Fig. 5(b) and 5(c)]. At the end of the first period of vibrations, the residual elastic energy allows the fluid to move clockwise inside the cell. Even in this case, the half-subharmonicity is evident from the map.

By cross comparison of Figs. 6(i) and 7(i), at this stage the reader will have realized that the two symmetries produce different behaviors in the spatiotemporal maps. Indeed, while for the (sa) symmetry the maps display three streaks, this number is reduced to two only for the (aa) symmetry. We will come back to this observation in the next section. As a concluding remark for this section, we discuss another effect related to the average energies reported in Fig. 5.

In particular, we wish to highlight that, while for the elastic energy, regardless of the value of ϑ, the inequality $\overline{EE}_{100} < \overline{EE}_{75} < \overline{EE}_{50}$ holds, a similar relationship cannot be easily deduced for $\overline{Nu}$ and (especially) for $\overline{K}$. Indeed, while at the onset of convection the inequality is true for all the averaged quantities, for $\vartheta = 0.1$, $\overline{Nu}_{75} > \overline{Nu}_{50}$ in a certain subrange of Ra_ω, while $\overline{Nu}_{100} < \overline{Nu}_{75}$ and $\overline{Nu}_{50}$, regardless of the considered value of Ra_ω. Similar results were also reported by Crewdson and Lappa [9] for Newtonian fluids in the range of small frequencies (see Fig. 10 and 11 in Ref. [9]). Although those authors analyzed the evolution of the maximum of the Nusselt number (here it is the time-averaged value), trends similar to that reported in the present study were obtained (which may be regarded as a possible hint for the existence of universality class in thermovibrational convection when it is considered in square cavities at low frequencies).

For what concerns the average kinetic energy, producing inequalities similar to the $\overline{EE}$ and $\overline{Nu}$ ones is not as straightforward as one would imagine. Indeed, this parameter is particularly affected when the bifurcation takes place. Moreover, since for every combination of (ϑ, Ω) the transition to a new solution occurs in different ranges of Ra_ω, abrupt jumps and intersecting lines are present in the graph in the central column of Fig. 5, which make such an attempt almost impossible. To elucidate further the significance of this observation, one should keep in mind that $\overline{K}$ accounts for the overall fluid field behavior, while $\overline{Nu}$ and $\overline{EE}$ consider only a subrange of the component of temperature gradient and extra stress tensor, respectively. Owing to this "component filtering," $\overline{Nu}$ and $\overline{EE}$ do not represent all the nonlinear effects that naturally emerge in the fluid. For the sake of completeness, here we wish to remark that a similar complexity in the trends of the K parameter has also been detected in studies dealing with RB convection, e.g., Zheng *et al.* [55].

C. Dynamic evolution of intermittent states

This subsection is finally devoted to the "intermittent" response, which, as mentioned earlier, we have detected for $(\vartheta, \Omega) = (0.10, 75), (0.20, 75), (0.10, 100)$, and $(0.15, 100)$. In order to do so, we analyze the signal of the velocity vertical
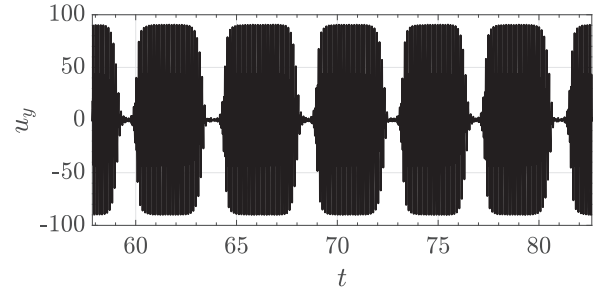

FIG. 8. Vertical component of the velocity probed in the center of the cavity for $\Omega = 100$, $\vartheta = 0.10$, and $Ra_\omega = 2.4 \times 10^4$.

component (u_y) probed in the center of the cavity $(x, y) = (0.5, 0.5)$ for the characteristic case of $\Omega = 100$, $\vartheta = 0.10$, and $Ra_\omega = 2.4 \times 10^4$ reported in Fig. 8. Such a figure is useful as it clearly shows that, in addition to the half-subharmonic variation of the signal, another long-period disturbance is affecting the flow evolution. The corresponding spatiotemporal map over the long period is reported in Fig. 9. Building on such plots and the observations about the patterning behavior for the two different convective modes made in Sec. IV B, we infer that, during the long period of oscillation (hereafter simply called secondary oscillation) the flow *intermittently* displays both a (sa) and (aa) symmetry (see the supplemental material [56] for the intermittent state video animation). The period of time in which a single mode is stable depends on the control parameters. Moreover, between each secondary oscillation, the flow becomes diffusive and stationary, i.e., the convective instabilities are temporally suppressed.

Most interestingly, the (angular) frequency ϖ of the secondary oscillation changes as a function of the vibrational Rayleigh number. This is shown in Fig. 10 where the variation of the angular frequency of the secondary oscillation is presented as a function of the reduced vibrational Rayleigh number $r(\vartheta, \Omega) = Ra_\omega / Ra_{\omega,cr}(\vartheta, \Omega)$, where $Ra_{\omega,cr}(\vartheta, \Omega)$ is the critical vibrational Rayleigh number for the onset of thermovibrational convection reported in Table II [used to represent all the four combination of (ϑ, Ω) in the same plot].

For $\Omega = 75$, the smallest frequency of the signal behaves as a linear function of r or, equivalently, Ra_ω. Increasing the vibrational frequency to 100 has the effect of producing a nonmonotonic law for the secondary oscillation frequency. Moreover, while for $\Omega = 75$ we observe the intermittent behavior only over a small range of Ra_ω, this fascinating mechanism is stable over a wider interval of the control parameter for $\Omega = 100$.
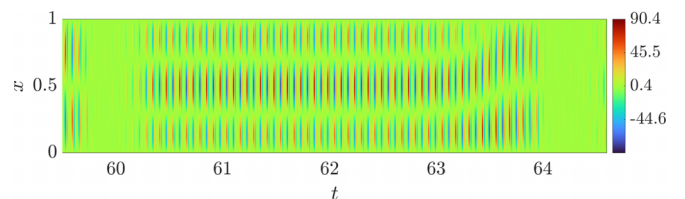

FIG. 9. Spatiotemporal map of the vertical component of the velocity (u_y) over the center-line orthogonal to the side-walls $(0 \leqslant x \leqslant 1$ and $y = 0.5)$ for $\Omega = 100$, $\vartheta = 0.10$, and $Ra_\omega = 2.4 \times 10^4$.
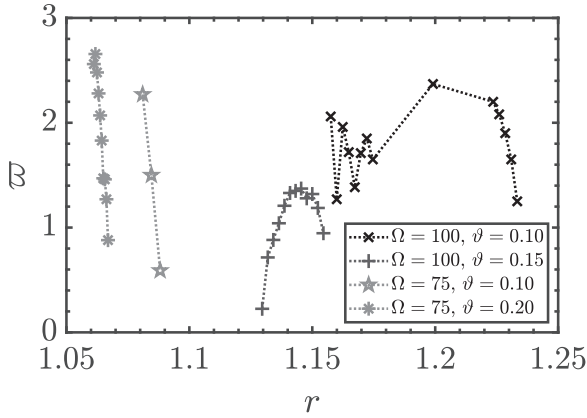
FIG. 10. Angular frequency ϖ of the secondary oscillation as a function of the reduced vibrational Rayleigh number $r = \text{Ra}_\omega/\text{Ra}_{\omega,\text{cr}}$.

Furthermore, a particular phenomenon shows up for the specific combination $(\vartheta, \Omega) = (0.20, 75)$, more specifically between the region of stability of the solution with the (sa) symmetry and the intermittent dynamics. A range of Ra_ω exists where the (aa) symmetry is stable. However, inspection of the related case depicted in Fig. 11, and its comparison with the "standard" symmetric (aa) state, lead to the conclusion that the center of rotation of the main cell oscillates horizontally with a low frequency. This state can be interpreted as a precursor of the state with intermittent evolution. Indeed, a relatively weak cell can be seen in the proximity of the left side $(x = 0)$, which is periodically suppressed by the bigger and stronger central vortex. This solution is stable for $1.653 \times 10^4 \leqslant \text{Ra}_\omega \leqslant 1.658 \times 10^4$.

In order to gain additional insights into the intermittent state, we have repeated some simulations by initializing them with the (sa) and (aa) solutions in place of the diffusive conditions. Remarkably, these additional computations have clarified that the unique regime in which the intermittent behavior occurs does not depend on the initial conditions or the specific path of evolution followed by the system. This apparent innocuous observation is instrumental in filtering out chaos-related aspects as possible root causes for the interpretation of this regime. Thermal flows in the "parallel" case are particularly prone to develop "multiple solutions," i.e., different states that can be entered for a fixed value of the control parameter depending on the initial conditions [2]. Generalized consensus exists in the literature that the competition among these attractors (existing in parallel in the space of parameters) can cause multifrequency states and ensuing transition to chaos. Behaviors of such a kind become even more frequent
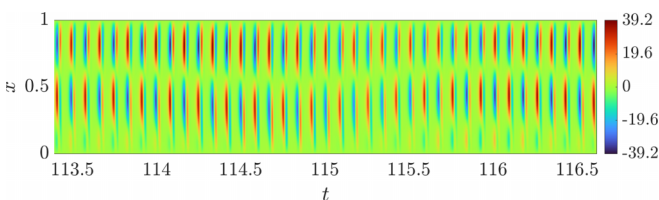
when viscoelastic fluids are considered, relevant examples in the case of of RB and MB convection being the works by Lappa and Boaro [23] and Lappa and Ferialdi [22].

Building on the the insensitivity of the "intermittent" state to the initial conditions and the fact that, on further increasing the control parameter a more regular behavior is recovered, however, we infer that this peculiar regime should be regarded as a meta-stable (quasiperiodic) condition in which the system continuously jump from one mode of convection to the other. In this regard, the same analogy already developed by Boaro and Lappa [25] with the resonant modes of convection identified by Rogers *et al.* [27] could be applied. Such peculiar mode of convection is driven by the coexistence of two distinct category of disturbances (each displaying a different temporal dependence), which are allowed to interact in a resonant way (Fig. 8).

V. CONCLUSIONS

Some general conclusions can be drawn as follows. Thermovibrational convection in the considered square cavity with vibrations parallel to the imposed temperature gradient is enabled as a threshold is exceeded in terms of Rayleigh number, which depends to a significant extent on the considered value of the elasticity number and the frequency of the forcing (the vibrations). While an increase in the frequency generally leads to a larger value of this critical parameter, a variation of the fluid elasticity can produce various trends depending on the considered frequency. The frequency also determines the emerging symmetry; in particular, two main categories of concurrent disturbances are at play in the considered region of the space of parameters.

On increasing the Rayleigh number, a unique hierarchy of bifurcations is produced where the initial symmetry displayed by the flow can be taken over by the concurrent one over a certain interval of the vibrational Rayleigh number. However, as a second threshold is exceeded the flow returns to its original symmetry.

Although this scenario applies to most of the situations considered, a subregion of the space of parameters exists where the competition of the two convective modes with different symmetries can give rise to an intermittent spatiotemporal behavior before a state with one or the other symmetry is recovered.

Future studies shall be devoted to assess the response of this flow in the three-dimensional case (cubic cavity) for which the number of possible symmetries is significantly enlarged and, therefore, more complex dynamics should be expected.

ACKNOWLEDGMENTS

FIG. 11. Spatiotemporal map of the vertical component of the velocity (u_y) over the center-line orthogonal to the side-walls $(0 \leqslant x \leqslant 1$ and $y = 0.5)$ for $\Omega = 75$, $\vartheta = 0.20$, and $\text{Ra}_\omega = 1.657 \times 10^4$.

[1] G. Z. Gershuni and A. V. Lyubimov, *Thermal Vibrational Convection* Vol. 1 (Wiley, England, 1998).

[2] M. Lappa, *Thermal Convection: Patterns, Evolution and Stability* (John Wiley & Sons, Ltd., Chichester, 2009).

[3] R. Savino and M. Lappa, Assessment of thermovibrational theory: Application to g-jitter on the space station, J. Spacecr. Rockets **40**, 201 (2003).

[4] A. Mialdun, I. I. Ryzhkov, D. E. Melnikov, and V. Shevtsova, Experimental evidence of thermal vibrational convection in a nonuniformly heated fluid in a reduced gravity environment, Phys. Rev. Lett. **101**, 084501 (2008).

[5] G. Z. Gershuni and E. M. Zhukhovitskii, Free thermal convection in a vibrational field under conditions of weightlessness, Sov. Phys. Doklady **24**, 894 (1979).

[6] S. Bouarab, F. Mokhtari, S. Kaddeche, D. Henry, V. Botton, and A. Medelfef, Theoretical and numerical study on high frequency vibrational convection: Influence of the vibration direction on the flow structure, Phys. Fluids **31**, 043605 (2019).

[7] A. N. Sharifulin, S. A. Plotnikov, and T. P. Lyubimova, Influence of the directions of vibrations and gravity on the formation of vortex structures of a nonuniformly heated fluid in a square cavity, Microgravity Sci. Technol. **34**, 97 (2022).

[8] K. Hirata, T. Sasaki, and H. Tanigawa, Vibrational effects on convection in a square cavity at zero gravity, J. Fluid Mech. **445**, 327 (2001).

[9] G. Crewdson and M. Lappa, The zoo of modes of convection in liquids vibrated along the direction of the temperature gradient, Fluids **6**, 30 (2021).

[10] G. Crewdson and M. Lappa, Spatial and temporal evolution of three-dimensional thermovibrational convection in a cubic cavity with various thermal boundary conditions, Phys. Fluids **34**, 014108 (2022).

[11] M. Renardy, High weissenberg number asymptotics and corner singularities in viscoelastic flows, in *IUTAM Symposium on Non-linear Singularities in Deformation and Flow*, edited by D. Durban and J. R. A. Pearson (Springer Netherlands, Dordrecht, 1999), pp. 13–20.

[12] H. Demir, R. W. Willianms, and F. T. Akyıldız, The singularities near the corner of a viscoelastic fluid in a 2d cavity, Math. Comput. Appl. **4**, 39 (1999).

[13] D. Siginer, *Stability of Non-Linear Constitutive Formulations for Viscoelastic Fluids*, SpringerBriefs in Applied Sciences and Technology (Springer, Berlin, 2014).

[14] R. G. Owens and T. N. Phillips, *Computational Rheology* (Imperial College Press, London, 2002).

[15] A. Bonito, P. Clément, and M. Picasso, Viscoelastic flows with complex free surfaces: Numerical analysis and simulation, in *Numerical Methods for Non-Newtonian Fluids*, Handbook of Numerical Analysis Vol. 16, edited by R. Glowinski and J. Xu (Elsevier, Amsterdam, 2011), pp. 305–369.

[16] M. Lappa, On the nature of fluid-dynamics, in *Understanding the Nature of Science*, Series: Science, Evolution and Creationism, edited by P. Lindholm (Nova Science Publishers Inc, 2019), Chap. 1, pp. 1–64.

[17] P. Kolodner, Oscillatory convection in viscoelastic dna suspensions, J. Non-Newtonian Fluid Mech. **75**, 167 (1998).

[18] M. Lappa, Thermally-driven flows in polymeric liquids, in *Encyclopedia of Materials: Plastics and Polymers*, edited by M. Hashmi (Elsevier, Oxford, 2022), pp. 724–742.

[19] J. Martinez-Mardones and C. Perez-Garcia, Linear instability in viscoelastic fluid convection, J. Phys.: Condens. Matter **2**, 1281 (1990).

[20] J. Martínez-Mardones and C. Pérez-García, Bifurcation analysis and amplitude equations for viscoelastic convective fluids, Il Nuovo Cimento D **14**, 961 (1992).

[21] Z. Li and R. E. Khayat, Finite-amplitude rayleigh-bénard convection and pattern selection for viscoelastic fluids, J. Fluid Mech. **529**, 221 (2005).

[22] M. Lappa and H. Ferialdi, Multiple solutions, oscillons, and strange attractors in thermoviscoelastic marangoni convection, Phys. Fluids **30**, 104104 (2018).

[23] M. Lappa and A. Boaro, Rayleigh-bénard convection in viscoelastic liquid bridges, J. Fluid Mech. **904**, A2 (2020).

[24] T. Lyubimova and K. Kovalevskaya, Gravity modulation effect on the onset of thermal buoyancy convection in a horizontal layer of the oldroyd fluid, Fluid Dyn. Res. **48**, 061419 (2016).

[25] A. Boaro and M. Lappa, Competition of overstability and stabilizing effects in viscoelastic thermovibrational flow, Phys. Rev. E **104**, 025102 (2021).

[26] M. Lappa and A. Boaro, Viscoelastic thermovibrational flow driven by sinusoidal and pulse (square) waves, Fluids **6**, 311 (2021).

[27] J. L. Rogers, W. Pesch, O. Brausch, and M. F. Schatz, Complex-ordered patterns in shaken convection, Phys. Rev. E **71**, 066214 (2005).

[28] A. Boaro and M. Lappa, Multicellular states of viscoelastic thermovibrational convection in a square cavity, Phys. Fluids **33**, 033105 (2021).

[29] D. X. Li, W. Liu, and D. Hao, Vibration antiresonance design for a spacecraft multifunctional structure, Shock Vib. **2017**, 5905684 (2017).

[30] M. P. Asir, A. Jeevarekha, and P. Philominathan, Multiple vibrational resonance and antiresonance in a coupled anharmonic oscillator under monochromatic excitation, Pramana J. Phys. **93**, 43 (2019).

[31] M. Lappa, The patterning behaviour and accumulation of spherical particles in a vibrated non-isothermal liquid, Phys. Fluids **26**, 093301 (2014).

[32] M. Lappa, Numerical study into the morphology and formation mechanisms of threedimensional particle structures in vibrated cylindrical cavities with various heating conditions, Phys. Rev. Fluids **1**, 064203 (2016).

[33] M. Lappa, On the multiplicity and symmetry of particle attractors in confined non-isothermal fluids subjected to inclined vibrations, Int. J. Multiphase Flow **93**, 71 (2017).

[34] M. Lappa, On the formation and morphology of coherent particulate structures in non-isothermal enclosures subjected to rotating g-jitters, Phys. Fluids **31**, 073303 (2019).

[35] M. Lappa and T. Burel, Symmetry breaking phenomena in thermovibrationally driven particle accumulation structures, Phys. Fluids **32**, 053314 (2020).

[36] G. Crewdson and L. Lappa, Thermally-driven flows and turbulence in vibrated liquids, Int. J. Thermofluids **11**, 100102 (2021).

[37] R. B. Bird, P. J. Dotson, and N. Johnson, Polymer solution rheology based on a finitely extensible bead-spring chain model, J. Non-Newton. Fluid Mech. **7**, 213 (1980).

[38] M. D. Chilcott and J. M. Rallison, Creeping flow of dilute polymer solutions past cylinders and spheres, J. Non-Newton. Fluid Mech. **29**, 381 (1988).

[39] W. M. Yang, Stability of viscoelastic fluids in a modulated gravitational field, Int. J. Heat Mass Transf. **40**, 1401 (1997).

[40] R. I. Issa, Solution of the implicitly discretised fluid flow equations by operator-splitting, J. Comput. Phys. **62**, 40 (1986).

[41] D. S. Jang, R. Jetli, and S. Acharya, Comparison of the piso, simpler, and simplec algorithms for the treatment of the pressure-velocity coupling in steady flow problems, Numer. Heat Transf. **10**, 209 (1986).

[42] F. Moukalled, L. Mangani, and M. Darwish, *The Finite Volume Method in Computational Fluid Dynamics: An Advanced Introduction with OpenFOAM and Matlab*, Fluid Mechanics and Its Applications, Vol. 113 (Springer, Cham, 2015), pp. XXIII, 791.

[43] C. M. Rhie and W. L. Chow, Numerical study of the turbulent flow past an airfoil with trailing edge separation, AIAA J. **21**, 1525 (1983).

[44] F. Pimenta and M. Alves, rheotool https://github.com/fppimenta/rheoTool (2016).

[45] F. Pimenta and M. A. Alves, Stabilization of an open-source finite-volume solver for viscoelastic fluid flows, J. Non-Newtonian Fluid Mech. **239**, 85 (2017).

[46] F. Pimenta and M. A. Alves, Conjugate heat transfer in the unbounded flow of a viscoelastic fluid past a sphere, Int. J. Heat Fluid Flow **89**, 108784 (2021).

[47] R. van Buel and H. Stark, Active open-loop control of elastic turbulence, Sci. Rep. **10**, 15704 (2020).

[48] R. Fattal and R. Kupferman, Constitutive laws for the matrix-logarithm of the conformation tensor, J. Non-Newton. Fluid Mech. **123**, 281 (2004).

[49] R. B. Bird, C. F. Curtiss, R. C. Armstrong, and O. Hassager, *Dynamics of Polymeric Liquids Vol. 2, 2nd ed.* (John Wiley & Sons, Chichester, 1987), pp. 1397–1398.

[50] M. A. Alves, P. J. Oliveira, and F. T. Pinho, Numerical methods for viscoelastic fluid flows, Annu. Rev. Fluid Mech. **53**, 509 (2021).

[51] A. Boaro and M. Lappa, On the competition of transverse and longitudinal modes of marangoni convection in a three-dimensional layer of viscoelastic fluid, Phys. Fluids **34**, 123103 (2022).

[52] N. Ouertatani, N. Ben Cheikh, B. Ben Beya, and T. Lili, Numerical simulation of two-dimensional Rayleigh-Bénard convection in an enclosure, C. R. Mec. **336**, 464 (2008).

[53] F. Stella and E. Bucchignani, Rayleigh-Bénard convection in limited domains: Part 1—Oscillatory flow, Numer. Heat Transf. A **36**, 17 (1999).

[54] J. Mizushima, Onset of the thermal convection in a finite two-dimensional box, J. Phys. Soc. Jpn. **64**, 2420 (1995).

[55] X. Zheng, F. Hagani, M. Boutaous, R. Knikker, S. Xin, and D. A. Siginer, Pattern selection in rayleigh-bénard convection with nonlinear viscoelastic fluids, Phys. Rev. Fluids **7**, 023301 (2022).

[56] See Supplemental Material at http://link.aps.org/supplemental/10.1103/PhysRevE.108.065101 for the video animation of the intermittent state reported in Figs. 8 and 9.

[57] A. Boaro and M. Lappa, Supplementary material for: "The symmetry properties and bifurcations of viscoelastic thermovibrational convection in a square cavity" (University of Strathclyde, 2023), Sq_cavity_parallel_file_for_Pure(.zip), doi:10.15129/f6e78c9e-9a43-467f-a4db-3dbfbfece700.